

# RSC Advances



This is an *Accepted Manuscript*, which has been through the Royal Society of Chemistry peer review process and has been accepted for publication.

*Accepted Manuscripts* are published online shortly after acceptance, before technical editing, formatting and proof reading. Using this free service, authors can make their results available to the community, in citable form, before we publish the edited article. This *Accepted Manuscript* will be replaced by the edited, formatted and paginated article as soon as this is available.

You can find more information about *Accepted Manuscripts* in the [Information for Authors](#).

Please note that technical editing may introduce minor changes to the text and/or graphics, which may alter content. The journal's standard [Terms & Conditions](#) and the [Ethical guidelines](#) still apply. In no event shall the Royal Society of Chemistry be held responsible for any errors or omissions in this *Accepted Manuscript* or any consequences arising from the use of any information it contains.



## Disposable Micro Stir Bars by Photodegradable Organic Encapsulation of Hematite-Magnetite Nanoparticles

Tina Zhang<sup>a</sup>, Paul Costigan<sup>a</sup>, Nitin Varshney<sup>a</sup>, Antonio Tricoli<sup>a†</sup>

Received 00th January 20xx,  
Accepted 00th January 20xx

DOI: 10.1039/x0xx00000x

www.rsc.org/

Development of high-throughput microfluidic systems requires engineering of novel miniaturized stirring concepts that can overcome diffusion-limited mixing in micro-vessels. Here, we present the facile and scalable fabrication of disposable magnetic micro stir bars by one-step photodegradable encapsulation of magnetically aligned iron oxide nanoparticle agglomerates with polylysine. The resulting superparamagnetic nanocomposites have a tunable aspect ratio and a nano-rough surface. Optimal composition and morphologies are determined over a broad set of self-assembly conditions leading to flexible elongated structures with excellent mixing performance. Rapid disassembly is demonstrated by in-situ photo-degradation of the coating under UV light providing a simple mean for their safe disposal.

### 1. Introduction

Lab-on-chip has become an enabling approach for an increasing number of applications including medical diagnostics,<sup>[1]</sup> study of cellular processes<sup>[2]</sup> and chemical synthesis<sup>[3]</sup>. However, engineering of high throughput systems requires rapid-mixing in confined, micro-scale channels and vessels. This is particularly challenging due to the intrinsically low Reynolds numbers at this scale that promote the establishment of laminar flows with diffusion-limited mass transfer profiles<sup>[4]</sup>. Mixing can be enhanced by passive means,<sup>[5]</sup> such as by channel shape-generated chaotic advection<sup>[6]</sup> and shortening the diffusion pathway by flow stream lamination<sup>[7]</sup>. Alternatively, mixing may be actively induced by application of external forces and fields such as by acoustic,<sup>[8]</sup> electrokinetic<sup>[9]</sup> and magnetic stimulation<sup>[10]</sup>.

Very recently, the utilization of magnetic micro- and nano-scale rods as miniaturized stir bars has been demonstrated as a flexible in-situ approach to overcome diffusion-limited mixing.<sup>[11]</sup> Top-down synthesis approaches for these structures are often based on micromachining technologies such as laser cutting<sup>[12]</sup> and lithography.<sup>[13]</sup> They result in quasi-monodisperse morphologies that are effective at improving sub-microliter mixing.<sup>[14]</sup> Development of bottom-up self-assembly approach has the potential to provide a more economically viable mean for their large-scale low-cost industrial production.

Self-assembly of micro stir bars has recently been achieved by silica encapsulation of magnetite nanoparticles<sup>[15]</sup>. This

resulted in chemically stable rod morphologies with high aspect ratio and excellent micro-scale mixing performance. A potential challenge remains their efficient disposal. Stiff one-dimensional nanostructures may have high cytotoxicity<sup>[16]</sup> and it is critical to avoid their dispersion in the environment. A safe approach is to engineer in-built mechanisms for easily induced disassembly. In this respect, the use of soft, degradable materials for their encapsulation can offer numerous advantages. In particular, amino acids, such as lysine, glutamate and peptides, have proven affinity for the surface of iron oxides.<sup>[17]</sup> They have been used to coat magnetic particles to create composite nanostructures for magnetically controlled delivery systems<sup>[18]</sup>. Polylysine, in particular, can easily bind with DNA<sup>[19]</sup> and numerous proteins<sup>[20]</sup>. Engineering of peptide-metal-oxide composite structure with an elongated micro-scale morphology may provide a multi-functional platform for lab-on-chip systems offering simultaneous mixing and targeted chemical delivery.<sup>[21]</sup>

Flame spray pyrolysis is a low-cost, scalable method for the production of both superparamagnetic (magnetite<sup>[22]</sup>) and ferromagnetic iron oxides (hematite<sup>[23]</sup>, maghemite<sup>[22]</sup> and wustite<sup>[22]</sup>) with tunable particle size and magnetic properties<sup>[24]</sup>. Magnetite and hematite are particularly interesting. The former has strong superparamagnetic properties with high saturation magnetization in the order of 50 emu/g for 10 nm nanoparticles<sup>[25]</sup> while the latter offers enhanced photocatalytic activity<sup>[26]</sup>. This has been exploited for applications in water splitting<sup>[27]</sup> and redox of carboxylic acids<sup>[28]</sup>. Both these iron oxides have high biodegradability at physiological conditions<sup>[29]</sup> and high affinity towards amino acids such as lysine<sup>[30]</sup>.

Here, we present a novel approach for the self-assembly of easily disposable micro-scale stirring bars via the one-step alignment of flame-made iron oxide nanocomposite particles and their *in situ* encapsulation with polylysine. Structural

<sup>a</sup> Nanotechnology Research Laboratory, Research School of Engineering, Australian National University, Canberra, Australia.

† Corresponding Author: Dr. Antonio Tricoli, antonio.tricoli@anu.edu.au  
Electronic Supplementary Information (ESI) available detailing: derivation of equation, material optimization and video footage of microbar rotation. See DOI: 10.1039/x0xx00000x

optimization is pursued over range of reaction pH, time, and magnetic field strength leading to a model of their anisotropic self-assembly. Their stirring performance is demonstrated by magnetically induced mixing of Trypan Blue dyes in aqueous solutions. Their rapid disassembly into the original iron oxide nanoparticles is achieved through the short application of UV light demonstrating a novel easily disposable material for improving the mixing performance of lab-on-chip systems.

## 2. Results and Discussion

### 2.1 Iron Oxide Synthesis

Crystalline iron oxide nanoparticles were synthesized in one-step by flame spray pyrolysis (FSP) of iron naphthenate in xylene solution. X-ray diffraction confirmed a predominant phase of superparamagnetic  $\text{Fe}_3\text{O}_4$  (magnetite) with residual ferromagnetic  $\alpha\text{-Fe}_2\text{O}_3$  (hematite). Although  $\alpha\text{-Fe}_2\text{O}_3$  (hematite) is more thermodynamically stable than  $\gamma\text{-Fe}_2\text{O}_3$  at moderate temperatures and pressures,<sup>[31]</sup> flame-synthesis is more commonly reported to produce  $\gamma\text{-Fe}_2\text{O}_3$  (maghemite)<sup>[32]</sup> than hematite,<sup>[33]</sup> due to the high cooling rates in spray flame reactors<sup>[22]</sup>. In contrast, thermal spray pyrolysis of acetylacetonate onto heated substrates has been commonly reported to yield hematite.<sup>[34]</sup> Here, the magnetite content of the nanopowders was between 70% and 100% as a function of the precursor concentration and dispersion oxygen (Fig. 1 a-c; Table 1). The as-prepared  $\text{Fe}_3\text{O}_4/\alpha\text{-Fe}_2\text{O}_3$  particles exhibited a quasi-spherical geometry and lognormal size distribution with a geometric standard deviation ( $\sigma_g$ ) of 1.15. The particle specific surface area was directly proportional to the concentration of Fe atoms fed to the gas phase (Table 1) as it has been previously remarked for the synthesis flame-made materials<sup>[35]</sup>. Increasing  $[\text{Fe}]/\text{O}_2$  from 0.3 to 1.5 mmol/L increased the BET particle diameter from 13 to 45 nm. Commercial magnetite nanoparticles had a predominantly cuboid geometry (Fig. 1c) with a log-normal shape size distribution with  $\sigma_g = 1.55$  and a mean diameter of 137 nm. Magnetic hysteresis was performed on the as-prepared iron oxide nanoparticles from +1 to -1 T (Fig. 1d). Both magnetic moment and remanence are key properties for application as stir bars. Structures of high saturation magnetization can be induced with a strong magnetic field and thus experience high torque in the presence of an external rotating magnetic field, an important characteristic to facilitate effective stirring. The saturation magnetization,  $M_s$ , obtained for the flame-made particles was between a maximum of 40 emu/g achieved at a  $[\text{Fe}]/\text{O}_2$  of 0.9 mmol/L (Fig. 1d, green line) and a minimum

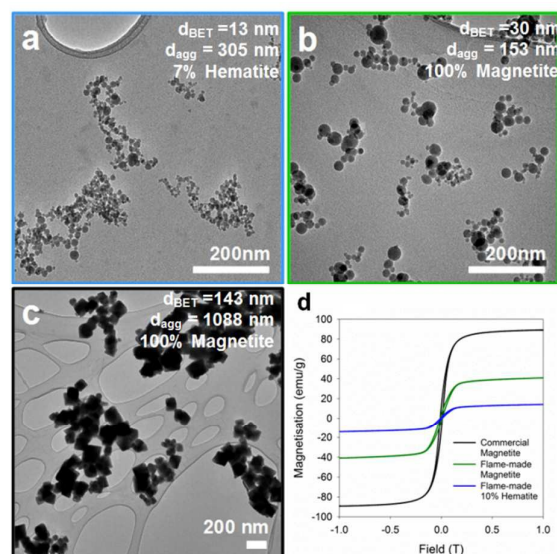


Fig. 1 TEM of iron oxide nanoparticles: flame-made iron oxide at (a) a  $[\text{Fe}]/\text{O}_2 = 0.3$  mmol/L, 7% Hematite, (b)  $[\text{Fe}]/\text{O}_2 = 0.9$  mmol/L, 100% Magnetite and (c) commercial magnetite. (d) Magnetic hysteresis of commercial magnetite (black line), flame-made 10% Hematite (blue line) and 100% Magnetite (green line).

of 10.2 emu/g at a  $[\text{Fe}]/\text{O}_2$  of 0.3 mmol/L (Fig. 1d, blue line). The saturation magnetization for all the flame-made samples was significantly lower than that of the commercial magnetite particles (90 emu/g). Overall, the magnetic moments observed here for the magnetite/hematite nanocomposites were comparable to those previously reported for flame-made materials ranging between 15-75 emu/g for mixtures of magnetite/maghemite/wustite<sup>[22]</sup> and 20-70 emu/g for predominantly maghemite<sup>[24]</sup>.

This is attributed to the strong dependence on the magnetic properties of iron oxide on both nanoparticle shape and size. The magnetic saturation is known to decrease sharply for particles below 10 nm.<sup>[36]</sup> An additional factor is the spherical shape of the particles produced here that is not commonly reported for flame-made iron oxides. Instead, it is more common to find faceted iron oxide as the product of flame-synthesis<sup>[22]</sup>. It is known that cubic magnetite has significantly higher saturation magnetization than spherical counterparts<sup>[37]</sup>. The hysteresis loops for the flame-made nanoparticles are largely superparamagnetic in shape with low remanence,  $M_r$  ( $M_r/M_s = 0.09$ ). Remanence values varied from 0.773 emu/g (Fig. 1d, blue line) to 3.70 emu/g (Fig. 1d, green line) for the flame-made iron oxides, and are significantly lower than the 9.41 emu/g of the commercial magnetite (Fig.

Table 1. Synthesis conditions and key structural properties of flame-made iron oxide nanoparticles.

$[\text{Fe}]/\text{O}_2$ (mmol/L)	Precursor Concentration (mol/L)	Precursor Flow Rate (mL/min)	Oxygen Flow Rate (L/min)	$d_{\text{BET}}$ (nm)	$d_{\text{agg}}$ (nm)	% Magnetite	$M_s$ (emu/g)
0.3	0.5	5	9	12.6	305	93	0.770
0.4	0.5	5	7	19.3		88	
0.5	0.5	5	5	15.2		67	
0.6	0.6	5	5	18.7		71	
0.9	0.6	3	2	30.2	153	98	3.70
1.5	0.6	5	2	45.0		94	

Dispersion oxygen pressure = 5 bar.

1d, black line). Low remanence is particularly important for application in micro stir bars as it enables the full demagnetization of the nanocomposite core when the magnetic field is removed. This permits particles to remain well-dispersed in the solution without exhibiting any strong ferromagnetic interactions.

Flame-made particles were agglomerates with a fractal-like structure due to Brownian coagulation and subsequent sintering within the high temperature residence time in the flame.<sup>[38]</sup> The agglomerate size is a critical dimension for the resulting particle mobility, and thus for the subsequent stir bars self-assembly. The agglomerate diameter of the flame-made and commercial nanoparticles were computed from the transmission electron micrographs (Fig. 1, a-c). Increasing the [Fe]/O<sub>2</sub> concentration from 0.3 to 0.9 mmol/L decreased the agglomerate size from 305 to 153 nm. The commercial magnetite particles had a mean agglomerate size of 1088 nm.

## 2.2 Microbar Self-Assembly

The flame-made iron oxide nanoparticles synthesized at a [Fe]/O<sub>2</sub> of 0.3 and 0.9 mmol/L were encapsulated with polylysine, a multi-functional organic partner for iron oxide that has shown applications in DNA condensation<sup>[19b, 39]</sup> and water friction reduction<sup>[40]</sup>. Encapsulation of iron oxide with polylysine was achieved in one-step by impregnation in L-lysine aqueous solutions as a function of different pH, lysine concentration and reaction time. The encapsulation of the iron oxide by polylysine is governed by the strong attraction between the positive amine groups of the amino acid and the negative surface of the iron oxide<sup>[41]</sup>. At the same time, the molecules of lysine have both acid and base character and have a strong intermolecular attraction. Thus, the iron oxide nanoparticles may be encapsulated at pH where both the iron oxide surface is negatively charged (pH > 7<sup>[42]</sup>) and the lysine is expressing amphoteric character (2.14 < pH < 12.48).

The resulting structures had a larger mean agglomerate size and density (Fig. 2). While the as-prepared flame-made iron oxides had an open fractal-like morphology (Fig. 1a,b), the

encapsulated agglomerates had a dense, close-packed structure resembling that previously reported for polypeptide-coated magnetic nanoparticles<sup>[43]</sup>.

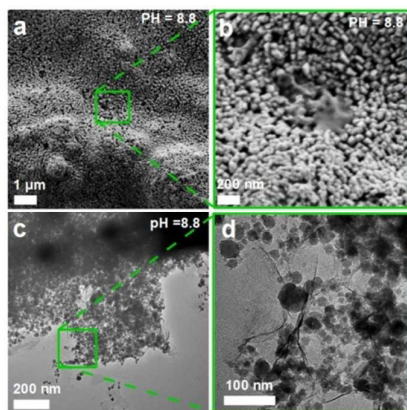


**Fig. 2** (a) SEM and (b) TEM images of flame-made magnetite ([Fe]/O<sub>2</sub> = 0.9 mmol/L) encapsulated in polylysine (PLL) at pH 8.8 showing a nanorough surface morphology.

In the absence of an externally applied magnetic field, the self-assembled microstructures had an isotropic growth, as evidenced by their optical and scanning electron micrographs (Fig. 3a), with a mean aspect ratio of ca. 1.8. By applying an external magnetic field perpendicular to the stirring plane and opposed to gravity, it was possible to promote anisotropic growth resulting in elongated structures of higher aspect ratios (Fig. 3b-d). The distance of the permanent magnet source and thus the strength of the applied magnetic field was found to have a strong effect on the resulting stir bar morphology. For the nanoparticles produced at [Fe]/O<sub>2</sub> of 0.3 mmol/L, decreasing the magnet-to-vessel distance from 10 to 2.5 cm increased the aspect ratio from 4.9 to 30 (Fig. 3b,c). While the micro-bar's width was not affected by the magnet distance for both experimental conditions, the average stir bar length increased drastically from 15 to 100 μm with decreasing magnet distance from at 10 to 2.5 cm. The saturation magnetization (Fig. 1d) had also an effect on the resulting self-assembly dynamics.

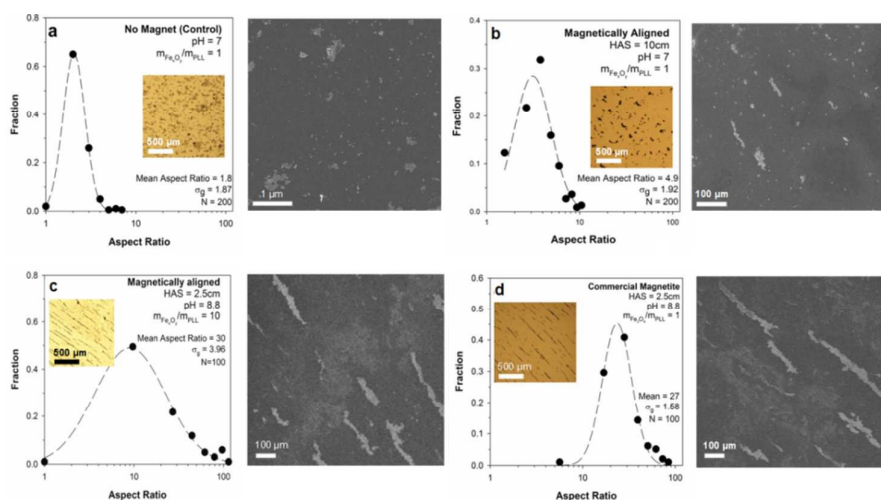


**Fig. 3** Aspect ratio distributions of encapsulated PLL-Fe<sub>3</sub>O<sub>4</sub> as computed from optical microscopy (inset) and scanning electron micrographs (beside) for flame-made iron oxide and commercial magnetite nanoparticles: (a) control with no magnetic alignment and (b,c) magnetically aligned flame-made Hematite-Magnetite nanoparticles ([Fe]/O<sub>2</sub> = 0.3 mmol/L), and (d) commercial magnetite.

## RSC Advances

In contrast, the reaction time, pH and lysine-to-iron oxide mass ratio were also investigated and found to have an overall lesser impact on the resulting structural properties (Supplementary Fig. S3) with aspect ratio increasing slightly with both reaction time and lysine content.

Comparison between the flame-made nanoparticles with a [Fe]/O<sub>2</sub> of 0.3 and 0.9 mmol/L showed a surprising trend. At the optimal encapsulation conditions of pH 8.8, iron oxide-to-lysine ratio ( $m_{\text{FeOx}}/m_{\text{PLL}}$ ) of 0.1, reaction time  $t_r$  of 24 h, magnet-to-vessel distance of 2.5 cm, longer chains were obtained with the a [Fe]/O<sub>2</sub> of 0.3 mmol/L samples despite their magnetic saturation (15 emu/g) being significantly lower than that (40 emu/g) of the samples with a [Fe]/O<sub>2</sub> of 0.9 mmol/L.

We propose that an additional important parameter driving self-assembly is the initial agglomerate size of the iron oxide nanoparticles. Although the samples with a [Fe]/O<sub>2</sub> of 0.3 mmol/L had a lower magnetic saturation (Fig. 1d), they also had a significantly larger agglomerate size (305 nm) than the samples with a [Fe]/O<sub>2</sub> of 0.9 mmol/L (153 nm). Assuming that self-assembly proceeds predominantly by end-on-end addition in the direction of the applied magnetic field, the final aspect is proportional the number of collisions between agglomerates along the direction of the applied field that result in successful adhesion. The agglomerate size has a two-fold effect on the collision frequency. Equation (1) describes the collision frequency  $Z_{AB}$  of agglomerate A, approximated as a sphere of radius  $r_A$ , and the end of one rod-shaped structure with a half thickness/radius  $r_B = r_A$ . The  $Z_{AB}$  is a function of the agglomerate radius and mean velocity of the colliding sphere  $v$ :

$$Z_{AB} = N_A N_B (r_A + r_B)^2 \pi v \quad (1)$$

Where  $Z_{AB}$  = collision frequency;  $v$  = velocity;  $N_A$  = number of colliding agglomerates with the bars;  $N_B$  = number of colliding bars with the agglomerate;  $r_A = r_B$  = agglomerate radius.

The velocity  $v$  can then be estimated by modelling the colliding agglomerate as a superparamagnetic sphere in a uniform magnetic field.<sup>[44]</sup> Only motion along the applied perpendicular magnetic field is considered here. This is equivalent to neglecting the influence of agglomerates and aligned microstructures on each other and assuming anisotropic growth only along the direction of the field. Agglomerate motion by diffusion is also neglected as the Péclet number is ca. 22 for this system indicating that ballistic motion along the magnetic field lines dominates.<sup>[45]</sup> The velocity term may be expressed by considering the balance of the accelerating magnetic force and the decelerating drag force acting on an agglomerate (supplementary equations S1 - S15). Thus, the collision frequency is given by:

$$Z_{AB} = 4N_A N_B r^2 \pi \left( C e^{-\frac{18\eta}{4r^2}t} + \frac{3\chi\mu m^2}{8\pi^2 x^5 \rho} \right) \quad (2)$$

With  $\eta$  = liquid dynamic viscosity,  $t$  = time elapsed,  $\chi$  = magnetic susceptibility of particle,  $\mu$  = permittivity of liquid,  $x$  = distance from magnet, and  $\rho$  = density of the agglomerate.

The exponential term can be neglected as the square dependency from the radius of agglomerates considered here ( $10^{-7}$  to  $10^{-6}$  m) results in values approaching zero. As a result, the collision frequency is dependent on the second power of the agglomerate diameter and directly proportional to their magnetic susceptibility. Supplementary Fig. S3 shows the plot of the normalized collision frequency ( $\frac{Z_{AB}}{N_A N_B}$ ) as a function of both agglomerate radius and magnetic susceptibility at normalized coordinates ( $t = 1$  s,  $x = 1$  cm). The results of this model suggest the critical impact of the agglomerate size when the magnetic susceptibility of the material is of similar magnitude, such as is the case for flame-made iron oxide nanoparticles. This effect may account for the higher aspect ratio of the sample with the higher initial agglomerate size (Fig. 3d) compared with the sample of lower agglomerate size (Fig. 3f).

The results also show the effect of magnetization of the starting nanoparticle material on the resulting microbar monodispersity. In all cases, the assembled microstructures possessed a greater geometric standard deviation compared with the initial nanomaterial, reflecting inhomogeneity inherent in the assembly procedure. However, the monodispersity was highest when the magnetization increased as for the commercial magnetite particles ( $\sigma_g = 1.58$ ) (Fig. 3d). The length of individual microbars relates directly to the size of its eddy when in rotation. Therefore, the geometric standard deviation of bars observed here will correlate to the dispersity in the size and speed of eddies during mixing. In turbulence, a wide distribution in eddy size and speed is typically observed. The wide distribution observed particularly for the flame-made sample ( $\sigma_g = 3.96$ ) (Fig. 3c) may render the material particularly suitable for turbulent mixing applications.

Finally, it was found that varying the reaction pH had a significant impact on the thickness and morphology of the polylysine encapsulating layer. At a pH of 4.65 and 7.4, the organic layer possessed a smooth morphology (Supplementary Fig. S2). In contrast, at pH of 8.8, the encapsulated structures had a nanorough surface morphology (Fig. 2). While the former has been reported before for polypeptide-encapsulated iron oxide<sup>[46]</sup> the latter presented here is novel. It is expected that the surface roughness of the encapsulated structures will increase their drag during magnetically induced rotation and is therefore an important pH-tunable characteristic of these hybrid organic-inorganic micro-bars.

### 2.3 Mixing Performance

The stirring performance of these micro-bars with a  $[\text{Fe}]/\text{O}_2$  of 0.9 mmol/L was assessed by two methods. First, time-lapse photography was used to monitor the vertical dispersion of Trypan Blue dye (Fig. 4). Magnetically induced rotation of the micro bars was compared to that of the randomly self-assembled agglomerates, and a control relying only on passive diffusion. The stirring effect of the aligned micro-bar structures was distinctly enhanced resulting in the near-complete dispersion of the dye after 7 min.

The dynamic behavior of the stirring bars was also investigated by continuous videos (Supporting Materials V1). It was found that the bars undergo two distinct modes of motion in the presence of a rotating field, in line with previous reports<sup>[15]</sup>. This was dependent on the distance from the center of rotation of the magnetic field. Bars closer to the center of the rotating field responded by rotating about their own center of mass, with no net motion. Those closer to the edge of the field responded by a shoal-like movement. In the first case, micro-scale vortices were generated resulting in turbulent mixing. Most notably, no in-situ flocculation of the micro bars into larger structures was observed, highlighting their stability in suspensions. Flocculation of magnetic structures in aqueous solutions is usually driven by interaction of induced magnetic fields between neighbouring particles. This is counterbalanced by the electrostatic repulsion induced

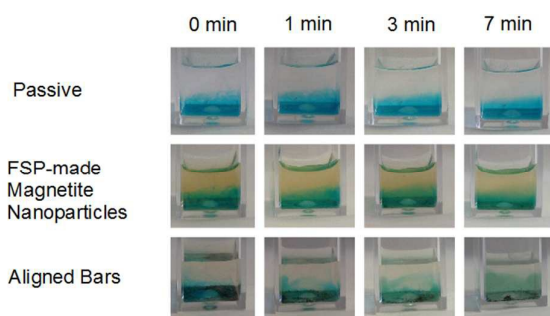


**Fig. 4** Time-lapse of vertical dye dispersion. (a) Passive (no iron oxide particles), (b) randomly oriented flame-made iron oxide nanoparticles ( $[\text{Fe}]/\text{O}_2 = 0.9$  mmol/L, 100% magnetite); (c) Aligned micro bars at a  $\text{pH} = 8.8$ ,  $t_r = 24\text{h}$ ,  $m_{\text{FeOx}}/m_{\text{PLL}} = 0.1$ ,  $\text{HAS} = 2.5\text{cm}$ .

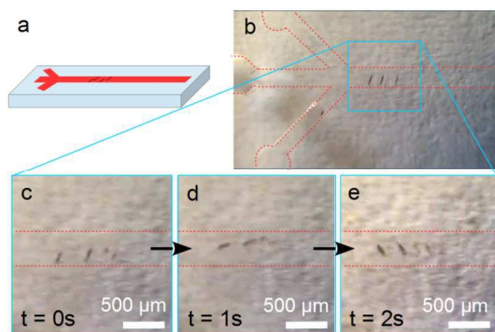


**Fig. 5** Rotation of magnetic microbars inside a microfluidic channel under an applied rotating field (1500 rpm). (a) Lab-on-chip schematic, (b) microbars within microchannel, (c–e) time lapse showing microbar rotation.

by the positively charged polylysine coatings that exists in protonated form in water ( $\text{NH}_3^+/\text{COO}^-/\text{NH}_3^+$ ). While it was not

possible to observe interactions between the micro bars containing flame-made particles with 90% magnetite, this was not the case for the bars assembled from commercial iron oxide particles. Their stronger saturation (90 emu/g) resulted in a significantly strong interactions and flocculation into large, millimeter scale structures.

This suggests that for application as micro stir bars there exists an optimal magnetic susceptibility. While high saturation is often preferred to maximize the torque, this also increase flocculation with neighboring micro-bars and thus a compromise is required to obtain stable and highly performing structures

We further demonstrated the direct application of the microbars within a microfluidic channel. A dilute suspension of the stirring bars was introduced into a standard PDMS chip. It was found that the use of a magnet is crucial to direct the microbars during injection into the chip to avoid blockage of the microchannel and to position the bars at the mixing point. The microbars rotated at 1500rpm with minimal horizontal travel. A series of screen captures is provided in below (Fig. 5). When applied within a dual stream system of water flowing beside trypan blue dye, the rotating microbars improved the mixing performance significantly. We observed an improved steady state diffusion profile across the width of the microchannel (Fig. 6b) compared with the low diffusion observed without the bars (Fig. 6a).

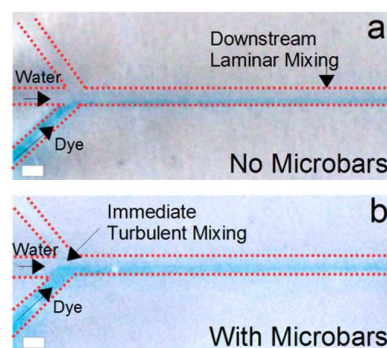


**Fig. 6** Steady State dye diffusion profiles within microchannel when (a) water is flowed beside trypan blue dye stream and (b) when microbars are present under an applied rotating magnetic field. Scale bar: 500µm.

## 2.4 Microbar Disassembly by UV Light

The disassembly of the micro stir bars was pursued by exposure to UV light. The molecular weight of polylysine is known to decrease upon exposure to UV due to the photocleavage of the peptide bonds. Iron oxides, and in particular hematite ( $\alpha\text{-Fe}_2\text{O}_3$ ), have been reported as a photoactive<sup>[47]</sup> materials with a relatively low bandgap of 1.9 - 2.2 eV (650 - 560 nm). This has been exploited for water splitting<sup>[48]</sup> and oxidation of aromatics<sup>[49]</sup>. Aqueous suspensions of the aligned encapsulated micro stir bars were exposed to sustained UV light at  $\lambda = 365$  nm and analyzed by optical microscope (Figure 7). The gradual degradation of the elongated structures was observed over a period of 5 min. The polylysine can be photocatalytically removed resulting in the destruction of the

microbar structure into agglomerates approximately one order of magnitude smaller in size. Their mean length decreased from 100 to 12  $\mu\text{m}$  while minimal change was observed for their mean diameter. This phenomenon is attributed to the direct degradation of polylysine coating on the  $\text{Fe}_3\text{O}_4/\text{Fe}_2\text{O}_3$  nanoparticle surface that results in the cleavage of polylysine bonds<sup>[50]</sup>. This is in line with the decomposition of polypeptide chains upon exposure to UV light in the presence of other photocatalytic nanoparticles, such as  $\text{TiO}_2$ .<sup>[51]</sup> Although some photocatalytic reactions on hematite surfaces have been reported including the formation of radicals from surface-bound organic molecules such as carboxylic acids,<sup>[28]</sup> iron oxides have not been investigated as catalysts for amino acid reactions. This mechanism has been exploited here for the first time for the rapid disassembly of high aspect ratio one-dimensional nanostructures facilitating their photo-induced disposal.

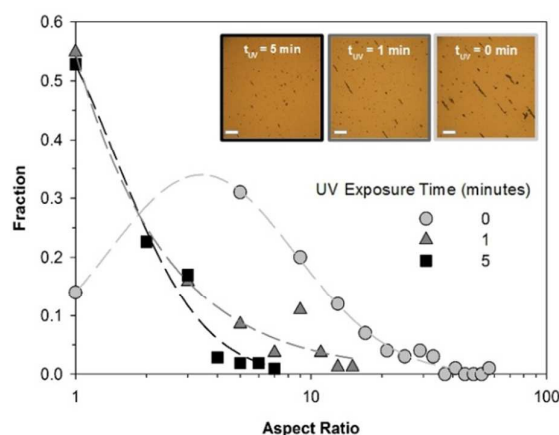


Fig. 7 Time-lapse optical microscopy of aligned microbars upon exposure to UV light. Scale bar: 100  $\mu\text{m}$ .

### 3. Conclusions

We have described a novel method for the one-step self-assembly of iron oxide nanoparticles into micro stir bars by polylysine encapsulation. The self-assembly dynamics was found to be strongly influenced by the strength of applied magnetic field, reaction pH, initial iron oxide agglomerate size, and magnetization properties such as susceptibility, saturation and remanence. The stirring behavior of these structures was investigated by dye dispersion. An optimal composition of the stirring bars was determined at lower saturation magnetization than previously reported. In fact, while high saturation magnetization supplies high torque, this is counterbalanced by the need for reducing magnetic attraction between the magnetized bars that would lead to flocculation and settling. The controllable UV-triggered disassembly of these micro stir bars was also demonstrated providing an easily disposable platform for lab-on-chip systems and micro-scale chemistry.

### 4. Experimental

#### 4.1 Flame Spray Pyrolysis

Iron oxide nanoparticles were synthesized using a flame spray pyrolysis (FSP) reactor (Supporting Materials, Figure S1) as previously reported. The liquid organometallic precursor containing of Fe-ions ( $0.5 - 0.6 \text{ mol L}^{-1}$ ) was prepared by mixing iron naphanate (Strem chemicals, 80% in mineral spirits) in Xylene (Fluka, purity > 98.5%). The solution was supplied through the FSP nozzle (at a rate of  $3 - 5 \text{ mL min}^{-1}$ ) and dispersed with oxygen at ( $2 - 9 \text{ L min}^{-1}$ ) with a pressure drop of 5 bar. The resulting fine spray was ignited by an annular pre-mixed methane/oxygen pilot flame ( $\text{CH}_4=1.2 \text{ L min}^{-1}$ ,  $\text{O}_2=2 \text{ L min}^{-1}$ ). Powder samples were collected with a vacuum pump (ICME Type M80B4) on water-cooled glass fiber filters (Sartorius glass microfiber FT-3-01124-150, 160mm diameter) placed at 40 cm height above the burner. The resulting iron oxide nanopowders were used without further purification.

#### 4.2 Encapsulation by Lysine

The magnetic micro-bars were synthesized by encapsulating the FSP-made iron oxide nanoparticles polylysine (PLL) in an aqueous buffer solution. The buffer composition and pH, and iron oxide/coating material mass ratios were altered. In all cases, 2 mg of iron oxide powder was added to 10 mL of deionized water / pH 4.65 acetate buffer (Sigma-Aldrich) / pH 7.4 phosphate buffered saline / pH 8.85 sodium borate buffer and mixed with appropriate mass of L-lysine (Sigma-Aldrich) according to the desired mass ratio formulation (0.2 mg, 2 mg and 20 mg). The resulting suspension was sonicated for 10 minutes, then wrapped in foil and placed on a stirring plate at 1500 rpm for 24 h, directly beneath a strong rare earth magnet supplying perpendicular vertical alignment field. The distance between the top of the stirring plate and the bottom of the perpendicular magnet (HAS) was set according to experimental conditions.

#### 4.3 Characterisation

**4.3.1 XRD.** X-ray diffraction analysis was performed with a Bruker D2 Phaser diffractometer operated at 30kV, 10mA at  $2\theta$  ( $\text{Cu K}\alpha$ ) =  $10^\circ - 80^\circ$ , step =  $0.02^\circ$  and scan speed  $2.3^\circ \text{ min}^{-1}$ . The crystal size ( $d_{\text{XRD}}$ ) was determined by Rietveld analysis with the structural parameters of identified iron oxide phases.

**4.3.2 BET.** The iron oxide powder specific surface area (SSA) was measured by BET analysis using a Micromeritics Tristar II after ca. 16 hours degassing under vacuum at  $120^\circ\text{C}$ . The BET equivalent diameter was calculated assuming primary particles and using the weighted average densities of iron oxide phases identified in the XRD analysis.

**4.3.3 Optical Microscopy.** The resulting micro-structures were imaged using optical microscope (Nikon Eclipse E200; TV lens 0.55x DS). Count distributions of mean bar length, width and aspect ratio were produced by measuring 200 bars for each sample using Image J software.

**4.3.4 Transmission Electron Microscopy.** Transmission Electron Microscopy was performed using Hitachi 7100 at 125kV.

#### 4.4 Stirring Performance

Vertical dye dispersion experiments were performed within standard polycarbonate cuvettes. 2.0 mL of aqueous solution (containing ca. 40 µg of particles/ microbars) was added to the cuvette. A solution of Trypan Blue (Sigma) was prepared by dissolving 2 mg in 20 mL of water containing 0.4 g of liquid soap. 0.2 mL of this dye solution was layered onto the bottom of the cuvette using a volumetric pipette (Gilson P1000). Stirring was applied at 1500 rpm using a stirring plate (IKAMAG).

Microchannel experiments were performed within a PDMS microfluidic chip, diameter 500 µm. A dilute aqueous suspension of bars (ca. 1 mg/ 20 mL) was pumped into the microfluidic channel at 0.5 bar pressure (AF1 dual-microfluidic and vacuum pump, Elveflow). A magnet was placed at the centre of the chip to position the particles at the mixing point. Stirring was applied at 1500 rpm and photography performed using an iPhone 4s. Water, Trypan blue dye (Sigma, 10mg/10mL in DI H<sub>2</sub>O) and dilute microbar suspension (2mg/10mL) streams were injected using syringe pumps (New Era Pumps) at 30µL/min. Rotation was once again performed at 1500 rpm (IKAMAG).

#### 4. 5 UV Light Exposure

UV light was applied on 1 mL aliquots of microbar suspensions using a UV lamp (Spectroline, 100W, 265nm).

#### Acknowledgements

The authors would like to acknowledge the following people: Miss Xuefei He of the Applied Optics Lab, The Australian National University, for her help in the microfluidic flow experiments; Dr Michael Cheah of the School of Biology, the Australian National University, for his advice; and Dr David Heslop of the Research School of Earth Sciences, the Australian National University, who performed the magnetic hysteresis experiments.

#### Notes and References

- V. Srinivasan, V. K. Pamula, R. B. Fair, *Lab Chip* **2004**, *4*, 310-315.
- H. Andersson, A. Van den Berg, *Sens. Actuators, B* **2003**, *92*, 315-325.
- E. M. Chan, R. A. Mathies, A. P. Alivisatos, *Nano Lett.* **2003**, *3*, 199-201.
- T. Thorsen, R. W. Roberts, F. H. Arnold, S. R. Quake, *Phys. Rev. Lett.* **2001**, *86*, 4163-4166.
- C. K. Chung, T. R. Shih, *Microfluid. Nanofluid.* **2008**, *4*, 419-425.
- P. Garstecki, M. A. Fischbach, G. M. Whitesides, *Appl. Phys. Lett.* **2005**, *86*, 244108.
- J. Branebjerg, P. Gravesen, J. P. Krog, C. R. Nielsen, *IEEE*, **1996**, pp. 441-446.
- K. Sritharan, C. Strobl, M. Schneider, A. Wixforth, Z. v. Guttenberg, *Appl. Phys. Lett.* **2006**, *88*, 054102.
- S. C. Jacobson, T. E. McKnight, J. M. Ramsey, *Anal. Chem.* **1999**, *71*, 4455-4459.
- L.-H. Lu, K. S. Ryu, C. Liu, *J. Microelectromech. Sys.* **2002**, *11*, 462-469.
- C.-Y. Lee, C.-L. Chang, Y.-N. Wang, L.-M. Fu, *Int. J. Mol. Sci.* **2011**, *12*, 3263-3287.
- D. De Bruyker, M. I. Recht, A. A. S. Bhagat, F. E. Torres, A. G. Bell, R. H. Bruce, *Lab Chip* **2011**, *11*, 3313-3319.
- K. S. Ryu, K. Shaikh, E. Goluch, Z. Fan, C. Liu, *Lab Chip* **2004**, *4*, 608-613.
- K. Zhang, Q. Liang, S. Ma, X. Mu, P. Hu, Y. Wang, G. Luo, *Lab Chip* **2009**, *9*, 2992-2999.
- W. H. Chong, L. K. Chin, R. L. S. Tan, H. Wang, A. Q. Liu, H. Chen, *Angew. Chem. Int. Ed.* **2013**, *125*, 8732-8735.
- H. Matsuzaki, M. Maeda, S. Lee, Y. Nishimura, N. Kumagai-Takei, H. Hayashi, S. Yamamoto, T. Hatayama, Y. Kojima, R. Tabata, T. Kishimoto, J. Hiratsuka, T. Otsuki, *J. Biomed. Biotechnol.* **2012**, *2012*, 9.
- S. Theerdhala, D. Bahadur, S. Vitta, N. Perkas, Z. Zhong, A. Gedanken, *Ultrason. Sonochem.* **2010**, *17*, 730-737.
- G. Minigo, A. Scholzen, C. K. Tang, J. C. Hanley, M. Kalkanidis, G. A. Pietersz, V. Apostolopoulos, M. Plebanski, *Vaccine* **2007**, *25*, 1316-1327.
- aM. L. Read, T. Etrych, K. Ulbrich, L. W. Seymour, *FEBS Lett.* **1999**, *461*, 96-100; bG. Liu, M. Molas, G. A. Grossmann, M. Pasumathy, J. C. Perales, M. J. Cooper, R. W. Hanson, *J. Biol. Chem.* **2001**, *276*, 34379-34387.
- B. L. Frey, C. E. Jordan, S. Kornguth, R. M. Corn, *Anal. Chem.* **1995**, *67*, 4452-4457.
- D. Y. Kwok, C. C. Coffin, C. P. Lollo, J. Jovenal, M. G. Banaszczyk, P. Mullen, A. Phillips, A. Amini, J. Fabrycki, R. M. Bartholomew, *BBA* **1999**, *1444*, 171-190.
- R. Strobel, S. E. Pratsinis, *Adv. Powder Technol.* **2009**, *20*, 190-194.
- F. Dillon, M. Copley, A. A. Koos, P. Bishop, N. Grobert, *RSC Adv.* **2013**, *3*, 20040-20045.
- D. Li, W. Y. Teoh, C. Selomulya, R. C. Woodward, P. Munroe, R. Amal, *J. Mater. Chem.* **2007**, *17*, 4876-4884.
- H. El Ghandoor, H. Zidan, M. M. Khalil, M. Ismail, *Int. J. Electrochem. Sci* **2012**, *7*, 5734-5745.
- Z. Cao, M. Qin, B. Jia, Y. Gu, P. Chen, A. A. Volinsky, X. Qu, *Ceram. Int.* **2015**, *41*, 2806-2812.
- K. Sivula, R. Zboril, F. Le Formal, R. Robert, A. Weidenkaff, J. Tucek, J. Frydrych, M. Gratzel, *J. Am. Chem. Soc.* **2010**, *132*, 7436-7444.
- I. A. Shkrob, S. D. Chemerisov, *J. Phys. Chem. C* **2009**, *113*, 17138-17150.
- F. M. Hilty, M. Arnold, M. Hilbe, A. Teleki, J. T. Knijnenburg, F. Ehrensperger, R. F. Hurrell, S. E. Pratsinis, W. Langhans, M. B. Zimmermann, *Nat. Nanotechnol.* **2010**, *5*, 374-380.
- aJ. Y. Park, E. S. Choi, M. J. Baek, G. H. Lee, *Mater. Lett.* **2009**, *63*, 379-381; bD. A. Zaia, H. J. Vieira, C. T. Zaia, *J. Braz. Chem. Soc.* **2002**, *13*, 679-681.
- J. Majzlan, K.-D. Grevel, A. Navrotsky, *Am. Mineral.* **2003**, *88*, 855-859.
- C. Janzen, P. Roth, *Combust. Flame* **2001**, *125*, 1150-1161.
- J. M. Mäkelä, H. Keskinen, T. Forsblom, J. Keskinen, *J. Mater. Sci.* **2004**, *39*, 2783-2788.
- J. B. Mooney, S. B. Radding, *Annu. Rev. Mater. Sci.* **1982**, *12*, 81-101.
- E. Lovell, J. Scott, R. Amal, *Molecules* **2015**, *20*, 4594-4609.
- D. Thapa, V. Palkar, M. Kurup, S. Malik, *Mater. Lett.* **2004**, *58*, 2692-2694.
- G. Zhen, B. W. Muir, B. A. Moffat, P. Harbour, K. S. Murray, B. Moubaraki, K. Suzuki, I. Madsen, N. Agron-Olshina, L. Waddington, P. Mulvaney, P. G. Hartley, *J. Phys. Chem. C* **2011**, *115*, 327-334.
- N. E. Motl, A. K. P. Mann, S. E. Skrabalak, *J. Mater. Chem. A* **2013**, *1*, 5193-5202.
- A. Mann, R. Richa, M. Ganguli, *Journal Control. Release* **2008**, *125*, 252-262.

## ARTICLE

Journal Name

- 40 S. Lee, M. Müller, M. Ratoi-Salagean, J. Vörös, S. Pasche, S. M. De Paul, H. A. Spikes, M. Textor, N. D. Spencer, *Tribol. Lett.* **2003**, *15*, 231-239.
- 41 M. Babic, D. Horák, M. Trchová, P. Jendelová, K. Glogarová, P. Lesný, V. Herynek, M. Hájek, E. Syková, *Bioconjugate Chem.* **2008**, *19*, 740-750.
- 42 R. A. Bini, R. F. C. Marques, F. J. Santos, J. A. Chaker, M. Jafellicci Jr, *J. Magn. Magn. Mater.* **2012**, *324*, 534-539.
- 43 L. E. Euliss, S. G. Grancharov, S. O'Brien, T. J. Deming, G. D. Stucky, C. B. Murray, G. A. Held, *Nano Lett.* **2003**, *3*, 1489-1493.
- 44 S. S. Shevkopyas, A. C. Siegel, R. M. Westervelt, M. G. Prentiss, G. M. Whitesides, *Lab Chip* **2007**, *7*, 1294-1302.
- 45 N. Nasiri, T. D. Elmoe, Y. Liu, Q. H. Qin, A. Tricoli, *Nanoscale* **2015**, *7*, 9859-9867.
- 46 G. Marcelo, A. Munoz-Bonilla, J. Rodriguez-Hernandez, M. Fernandez-Garcia, *Polymer Chem.* **2013**, *4*, 558-567.
- 47 F. Le Formal, M. Grätzel, K. Sivula, *Adv. Funct. Mater.* **2010**, *20*, 1099-1107.
- 48 K. Sivula, F. Le Formal, M. Grätzel, *Chem. Sus. Chem.* **2011**, *4*, 432-449.
- 49 T. Imai, T. Matsui, Y. Fujii, T. Okita, T. Nakai, *Nippon Kagaku Kaishi* **2000**, 541-546.
- 50 T. Zhang, M. A. Go, C. Stricker, V. R. Daria, A. Tricoli, *J. Mater. Chem. B* **2015**, *3*, 1677-1687.
- 51 H. Hidaka, S. Horikoshi, K. Ajisaka, J. Zhao, N. Serpone, *J. Photochem. Photobiol. A* **1997**, *108*, 197-205.